Order parameter for bursting polyrhythms in multifunctional central pattern generators

Jeremy Wojcik, Robert Clewley, and Andrey Shilnikov

Phys. Rev. E **83**, 056209 — Published 16 May 2011

DOI: 10.1103/PhysRevE.83.056209

Order parameter for bursting polyrhythms in multifunctional central pattern generators

Jeremy Wojcik, Robert Clewley, and Andrey Shilnikov
Neuroscience Institute and Department of Mathematics and Statistics, Georgia State University, Atlanta, GA 30303, USA

We examine multistability of several coexisting bursting patterns in a central pattern generator network composed of three Hodgkin-Huxley type cells coupled reciprocally by inhibitory synapses. We establish that control of switching between bursting polyrhythms and their bifurcations are determined by the temporal characteristics, such as the duty cycle, of networked interneurons and the coupling strength asymmetry. A computationally effective approach for the reduction of dynamics of the 9D network to 2D Poincaré return mappings for phase lags between the interneurons is presented.

PACS numbers: 05.45.Xt, 87.19.L-

A central pattern generator (CPG) is a neural microcircuit of cells whose synergetic interactions, without sensory input, rhythmically produce patterns of bursting that determine motor behaviors such as heartbeat, respiration, and locomotion in animals and humans [1]. While a dedicated CPG generates a single pattern robustly, a multifunctional CPG can flexibly produce distinct rhythms, such as temporarily distinct swimming versus crawling, and alternation of blood circulation patterns in leeches [2, 3]. Switching between such rhythms is attributed to input-dependent switching between attractors of the CPG.

Here we analyze multistability and transformations of rhythmic patterns in a 9D model of a CPG motif (Fig. 1) comprised of 3 endogenously bursting leech heart interneurons [4] coupled (reciprocally) by fast inhibitory chemical synapses [5]. Our use of fast threshold modulation [6] implies that the post-synaptic current is zero (resp., maximized) when the voltage of a driving cell is below (resp., above) the synaptic threshold. This is an inherently bi-directionally asymmetric form of coupling. Many anatomically and physiologically diverse CPG circuits involve a 3-cell motif [7], including the spiny lobster pyloric network, the *Tritonia* swim circuit, and the *Lymnaea* respiratory CPGs [8]. We show how rhythms of the multistable motif are selected by changing the relative timing of bursts by physiologically plausible perturbations. We also demonstrate how the set of possible rhythmic outcomes can be controlled by varying the duty cycle of bursts, and by varying the coupling around the ring.

We propose a novel computational tool for detailed examination of polyrhythmic bursting in biophysical CPG models with coupling asymmetries and arbitrary coupling strength. The tool reduces the problem of stability and existence of bursting rhythms in large networks to the bifurcation analysis of fixed points (FP) of Poincaré return mappings for phase lags. Our approach is based on delayed release of cells from a suppressed state, and complements the phase resetting techniques allowing for for thorough exploration of network dynamics with spiking cells [9]. It demonstrates that more general inhibitory networks possess stable bursting patterns that do not occur in similar 3-oscillator motifs with gap-junction coupling, which is bi-directionally symmetric [10].

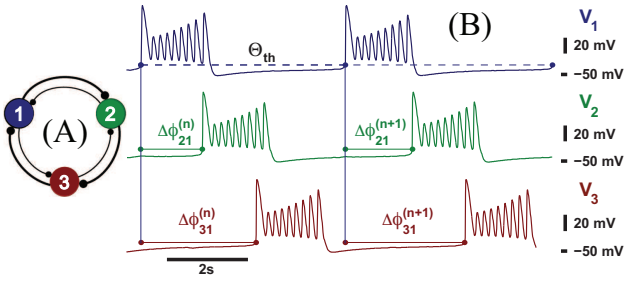

FIG. 1. (Color online) (A) 3-cell motif with asymmetric clockwise versus counter-clockwise connection strengths. (B) Voltage traces: the phase (mod 1) of reference cell 1 (blue) is reset when V_1 reaches threshold $\Theta_{\rm th} = -40$ mV. The time delays between the burst onset in the reference cell 1 and the burst onset in cells 2 (green) and 3 (red), normalized over the recurrent time of cell 1, define a sequence of phase lags $\{\Delta\phi_{21}^{(n)}, \Delta\phi_{31}^{(n)}\}$.

The duty cycle (DC) of bursting, being the fraction of the burst period in which cells spike, is turned out to be an order parameter that regulates motif synchronization properties [5, 11]. The DC is sensitive to fluctuations of most cell's intrinsic parameters, and is affected by applied and synaptic currents [4, 5]. We treat DC implicitly as a bifurcation parameter that defines *short* (DC∼20%), *medium* (DC∼50%), and *long* (DC∼80%) bursting motifs. DC is controlled by an intrinsic parameter of the interneuron that shifts the activation of the potassium current in the leech heart interneuron.

In this study we consider an adequately "weakly" coupled motif using the nominal value of a maximal conductance $\tilde{g}_{\rm syn} = 5 \times 10^{-4}$ nS. This coupling strength guaranties relatively slow convergence of transients to phase-locked states of the motif, and hence permits us to visualize "smooth" trajectories that expose in detail

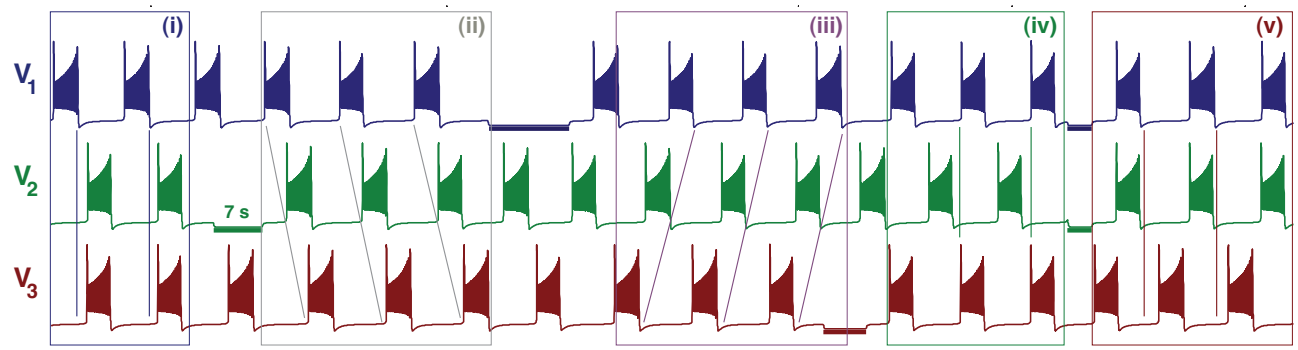

FIG. 2. (Color online) 5 polyrhythms in the medium bursting motif at $g_{\rm syn} = 5 \times 10^{-3}$ (increased to secure short transients for the purpose of illustration). Inhibitory pulses (horizontal bars) suppress the targeted cells, thus causing switching between co-existing rhythms: $(1 \perp \{2 \parallel 3\})$ in episode (i), traveling waves $(1 \prec 2 \prec 3)$ in (ii) and $(1 \prec 3 \prec 2)$ in (iii), followed by $(2 \perp \{1 \parallel 3\})$ led by cell 2 in (iv). Having released cells 1 and 2 simultaneously, cell 3 leads the motif in the $(3 \perp \{1 \parallel 2\})$ rhythm in the last episode.

the structure of phase-lag return maps, qualitatively resembling time-continuous planer vector fields in this case. The findings obtained for this case prepare the basis for understanding more complex patterns in strongly coupled, non-homogeneous motifs with the same technique. The asymmetry of the motif is governed by another bifurcation parameter $g_{\circlearrowleft}$, which weakens (resp., enforces) counter-clockwise (resp., clockwise) coupling strengths $g_{\rm c}^{\rm cc} = \tilde{g}_{\rm syn}(1 \mp g_{\circlearrowleft})$, $0 \geq g_{\circlearrowleft} \leq 1$, from the nominal value $\tilde{g}_{\rm syn}$.

As the period of network oscillations can fluctuate in time, we define delays between the onset of bursting in cell 2 (green) and cell 3 (red) relative to that in the the reference cell 1 (blue) at the instances the voltages V_i increase through a threshold of $\Theta_{\rm th} = -40$ mV (Fig. 1). Initial delays are controlled by the timely release of cells 2 and 3 from inhibition (Fig. 2). The subsequent delays normalized over the period of the cell 1 define a sequence or forward trajectory $\left\{\Delta\phi_{21}^{(n)}, \Delta\phi_{31}^{(n)}\right\}$ of phase-lag return maps on a torus $[0,1) \times [0,1)$ with $\Delta\phi_{i1}$ mod 1. The maps are tabulated on a 40×40 (or more) grid of initial points. The iterates are connected in Figs. 3–5 to preserve order. We then study the dynamical properties of the maps, locate fixed points and evaluate their stability, detect periodic and heteroclinic orbits, and identify the underlying bifurcations as the parameters, DC and $g_{\circlearrowleft}$, are varied.

Fig. 3A shows the $(\Delta\phi_{31}, \Delta\phi_{21})$ phase-lag map for the S_3-symmetric, medium bursting motif. The map has five stable FPs corresponding to the coexisting phase-locked rhythms: the (red) FP at $(\Delta\phi_{31} \approx \frac{1}{2}, \Delta\phi_{21} \approx 0)$, the (green) FP $(0, \frac{1}{2})$, the (blue) FP $(\frac{1}{2}, \frac{1}{2})$, and the (black) FP $(\frac{2}{3}, \frac{1}{3})$ and the (purple) FP $(\frac{1}{3}, \frac{2}{3})$. The attraction basins of the FPs are divided by separatrices (incoming and outgoing sets) of six saddles (small grey dots in the phase diagrams). The neighborhood of (0,0) has a complex structure at high magnification (not shown), but is effectively repelling. Locations of the FP do not correspond to exact fractions due to overlap and interaction between bursts and a slight ambiguity in the measurement and definition of momentary phases.

The coordinates of the FPs determine the phase locked states within bursting rhythms of the motif that are denoted symbolically as follows: $(1 \prec 2 \prec 3)$ and $(1 \prec 3 \prec 2)$ for clockwise and counter-clockwise traveling waves of bursting (resp.) around the ring (episodes (ii) and (iii) of the voltage trace in Fig. 2) corresponding to the FPs located near $(\frac{1}{3}, \frac{2}{3})$ and $(\frac{2}{3}, \frac{1}{3})$, respectively.

Besides these rhythms (which stability is unknown *a priori*) in a symmetric motif, the three other FPs correspond to the rhythms where one cell fires in anti-phase ($\Delta\phi \sim \frac{1}{2}$, or $\perp$) against two cells bursting simultaneously in-phase ($\Delta\phi = 0$, or $\parallel$). The stable FP at $(\frac{1}{2}, \frac{1}{2})$ corresponds to the $(1 \perp \{2 \parallel 3\})$-pattern (episode (i) of Fig. 2); FP $(0, \frac{1}{2})$ corresponds to $(2 \perp \{1 \parallel 3\})$-pattern (episode (iv)); and FP $(\frac{1}{2}, 0)$ corresponds to $(3 \perp \{1 \parallel 2\})$-pattern (episode (v)). We note that such anti-phase patterns are recorded at switches between peristaltic and synchronous rhythms in the leech heartbeat CPG [3] and in the *Tritonia* CPG during escape swimming [8].

The selection of rhythmic outcome in a multifunctional motif depends on the initial phase distributions of the cells. Evaluation of the FP attraction basins in Fig. 3A suggests that when the cells are simultaneously released from external inhibition, e.g. with initial phases reset, the medium bursting motif can generate one of five robust rhythms with nearly equal odds. The geometry of the phase-lag map also informs how to switch the motif to a specific rhythm by perturbing it in a certain phase direction, i.e. advancing or delaying cells. A biophysically plausible way to control switching is to apply an appropriately-timed hyperpolarizing pulse to temporarily suppress a targeted cell(s). Fig. 2 demonstrates the approach for the symmetric, medium bursting motif.

Comparison of the maps for the symmetric motifs in

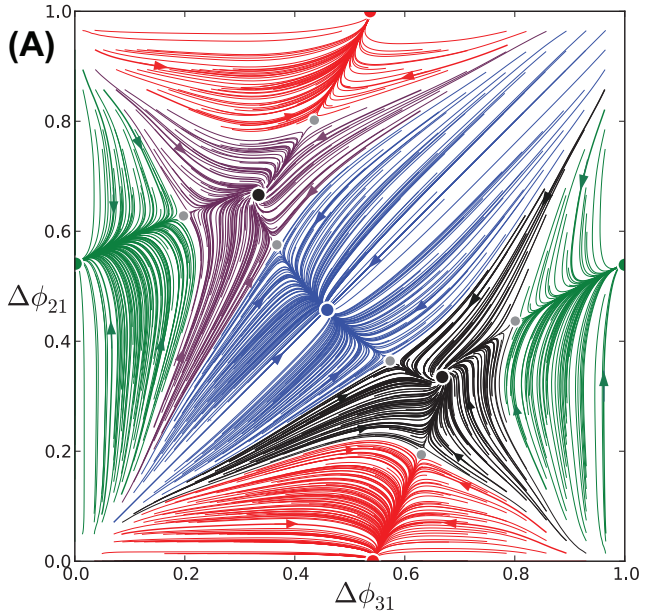

FIG. 3. (Color online) (A) Phase-lag map for the symmetric, medium bursting motif showing five stable FPs: (red) dot at $\sim (\frac{1}{2}, 0)$, (green) $(0, \frac{1}{2})$, (blue) $(\frac{1}{2}, \frac{1}{2})$, (black) $(\frac{2}{3}, \frac{1}{3})$ and (purple) $(\frac{1}{3}, \frac{2}{3})$, corresponding to the anti-phase $(3 \perp \{1 \parallel 2\})$, $(2 \perp \{1 \parallel 3\})$, $(1 \perp \{2 \parallel 3\})$ bursts, and traveling clockwise $(1 \prec 2 \prec 3)$ and counter-clockwise $(1 \prec 3 \prec 2)$ waves; the attraction basins are divided by "separatrices" (stable sets) of six saddles (small grey dots). Arrows indicate the forward iterate direction in the phase plane. (B) Asymmetric motif at $g_{\circlearrowright} = 0.154$ near the saddle-node bifurcations annihilating three stable FPs for anti-phase bursting rhythms.

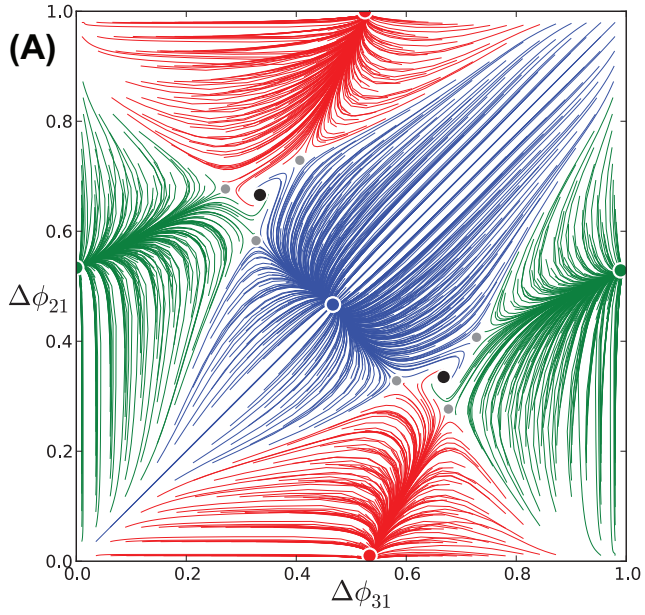

FIG. 4. (Color online) (A) Phase-lag map for the symmetric, short bursting motif showing only 3 stable FPs (blue dot at $(\frac{1}{2}, \frac{1}{2})$, red dot at $(\frac{1}{2}, 0)$, and green dot at $(0, \frac{1}{2})$) corresponding to anti-phase rhythms where one cell bursts followed by synchronized bursts in the other two cells. Unstable FPs at $(\frac{2}{3}, \frac{1}{3})$ and $(\frac{1}{3}, \frac{2}{3})$ exclude the clockwise $(1 \prec 2 \prec 3)$ and counter-clockwise $(1 \prec 3 \prec 2)$ traveling waves from the repertoire of the short bursting motif. (B) Map for the asymmetric motif $(g_{\circlearrowright} = 0.2)$ depicting a stable invariant curve near a three-saddle connection around the FP at $(\frac{2}{3}, \frac{1}{3})$.

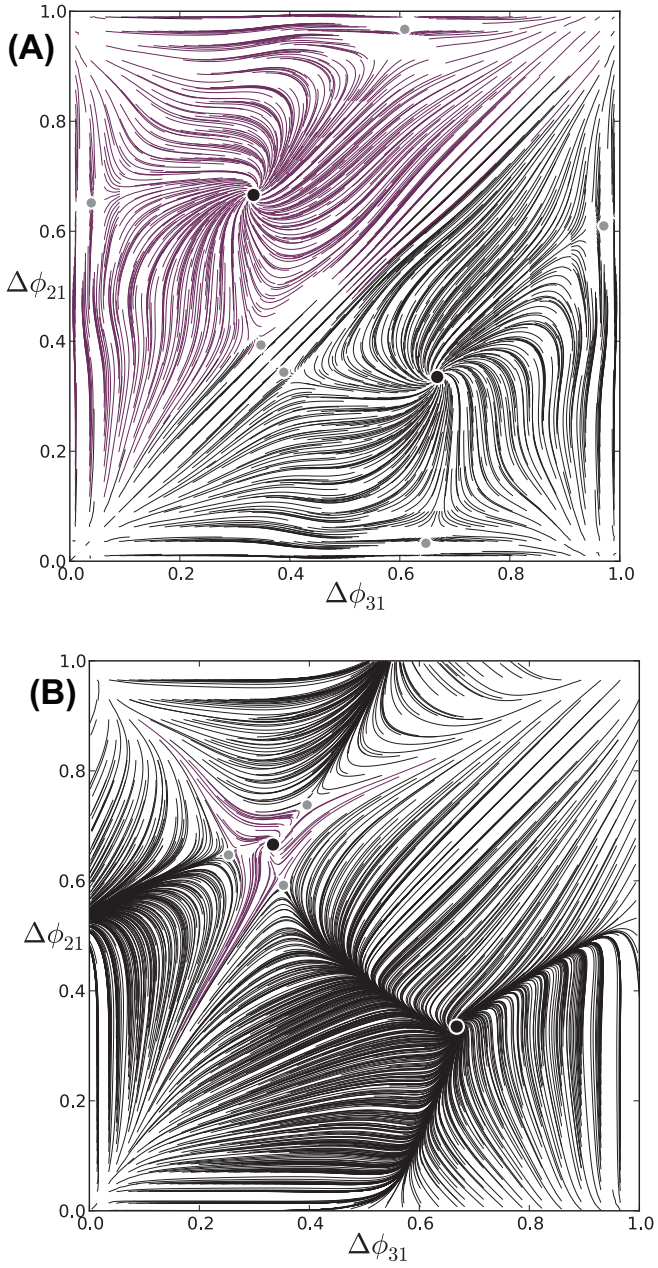

FIG. 5. (Color online) (A) Phase-lag map for the symmetric, long bursting motif revealing two equally dominant attractors: $(\frac{2}{3},\frac{1}{3})$ and $(\frac{1}{3},\frac{2}{3})$ for $(1\prec 2\prec 3)$ and $(1\prec 3\prec 2)$ traveling rhythms. (B) Map for the asymmetric ($g_{\circlearrowleft}=0.3$) medium bursting motif depicting two persistent attractors: the one for the clockwise $(1\prec 2\prec 3)$ rhythms prevails over the attractor for the counter-clockwise $(1\prec 3\prec 2)$ rhythm. Further increase in $g_{\circlearrowleft}$ leads to the only observable $(1\prec 2\prec 3)$ rhythm, after FP at $(\frac{1}{3},\frac{2}{3})$ merges with 3 nearby saddles.

cases of medium (Figs. 3, 5B), short (Fig. 4) and long (Fig. 5A) bursting demonstrates that DC is a physiologically plausible parameter that determines the dominant observable rhythms. I.e., short bursting makes it impossible for both clockwise $(1\prec 2\prec 3)$ and counter-clockwise $(1\prec 3\prec 2)$ traveling wave patterns to occur in the symmetric motif as the corresponding FPs are unstable initially. In contrast, the symmetric long bursting motif is unlikely to generate anti-phase rhythms, as the corresponding FPs have narrow attraction basins, divided equally between the FPs corresponding to the traveling waves.

We examine next the bifurcations of FPs of the phase-lag map as the motif becomes Z_3-rotationally (a)symmetric by increasing $g_{\circlearrowleft}$, which weakens counter-clockwise and enforces clockwise-directed synapses. The limit $g_{\circlearrowleft}\to 1$ makes the motif unidirectionally coupled with only the $(1\prec 2\prec 3)$ rhythm observable. Here, the FP at $(\frac{2}{3},\frac{1}{3})$ expands its attraction basin over the entire phase range. Intermediate stages of structural transformation of the phase-lag map for the medium bursting motif are demonstrated in Figs. 3 and 5B. First, as $g_{\circlearrowleft}$ increases to 0.154, the three saddles move away from the FP at $(\frac{2}{3},\frac{1}{3})$, thereby increasing its attraction basin, and approach the stable FPs corresponding to anti-phase bursting rhythms. Meanwhile, the other three saddles move towards the FP at $(\frac{1}{3},\frac{2}{3})$ corresponding to the $(1\prec 3\prec 2)$ rhythm, narrowing its basin. As $g_{\circlearrowleft}$ is increased further, the attractors and saddles in the bottom right of the unit square merge and vanish through saddle-node (SN) bifurcations. Increasing $g_{\circlearrowleft}$ makes the FP $(\frac{2}{3},\frac{1}{3})$ for the $(1\prec 2\prec 3)$ rhythm globally dominant (Fig. 5B) after the three nearby saddles collapse onto the FP at $(\frac{1}{3},\frac{2}{3})$. Bifurcations in the long bursting motif are similar, except that the SN bifurcation occurs at smaller $g_{\circlearrowleft}$ values.

The bifurcation sequence in the short bursting motif is qualitatively different: the SN bifurcations occur at a higher degree of asymmetry ($g_{\circlearrowleft}\approx 0.48$), delayed by another bifurcation that makes the clockwise traveling pattern the global attractor of the motif. To become stable, the corresponding FP at $(\frac{2}{3},\frac{1}{3})$ undergoes a secondary supercritical Andronov-Hopf or torus bifurcation. Fig. 4B depicts the map at $g_{\circlearrowleft}=0.2$ showing a stable invariant curve near the heteroclinic connections between the three saddles around the given FP. The invariant curve is associated with the appearance of slow phase jitters within the $(1\prec 2\prec 3)$ rhythm in voltage traces. Once it collapses onto the FP at $(\frac{2}{3},\frac{1}{3})$ the asymmetric motif gains a new robust $(1\prec 2\prec 3)$ rhythm, making four possible bursting outcomes.

The stability of the FPs in the phase-lag maps is *de facto* proof of the observability of the matching rhythmic outcomes generated by a motif, symmetric or not. While the existence of some rhythms, like generic $(1\prec 2\prec 3)$ and $(1\prec 3\prec 2)$, in a 3-cell motif can hypothetically be deduced using symmetry arguments, the robustness and observability of the rhythms must be justified by accurate

computational verification, as their stability strongly correlates with the temporal properties of the bursting cells. Using the proposed computational technique for the reduction of dynamics of the 9D 3-cell motif to the analysis of the equationless 2D mappings for the phase lags between the bursting cells, we have demonstrated that a reciprocally inhibitory (non)homogeneous network can be multistable, i.e. can generate several distinct polyrhythmic bursting patterns. It is shown for the first time that the observable rhythms of the 3-cell motif are determined not only by its (a)symmetry, but the duty cycle serving the role of the order parameter for bursting networks. This knowledge of the existence, stability and possible bifurcations of polyrhythms in this 9D motif composed of the interneuron models is vital for derivations of reduced, phemenologically accurate phase-models for nonhomogeneous biological CPGs with mixed, inhibitory and excitatory synapses.

We thank W. Kristan, A. Neiman, P. Ashwin, C. Laing and R. Lin for valuable suggestions, and M. Brooks for taking part in the pilot phase of the project. We acknowledge support from NSF Grants CISE/CCF-0829742 (to R.C.), DMS-1009591 and RFFI Grant No. 08-01-00083 (to A.S.), and the GSU Brains & Behavior program.

found in the supplement.

[1] A. Selverston (ed), *Model Neural Networks and Behavior*, (Springer, 1985); F. Skinner, N. Kopell, E. Marder, *Comput. Neurosci.* **1**, 69 (1994); E. Marder, R. L. Calabrese, *Physiol. Rev.* **76**, 687 (1996); N. Kopell, G. B. Ermentrout, *PNAS USA* **101**, 15482 (2004).

[2] K. L. Briggman, W. B. Kristan, *Annu. Rev. Neurosci.* **31** (2008).

[3] W. B. Kristan, R. L. Calabrese, W. O. Friesen, *Prog. Neurobiol.* **76**, 279 (2005); A. Weaver, R. Roffman, B. Norris, R. Calabrese, *Frontiers in Behav. Neurosci.* **4**(38), 1 (2010).

[4] A. Shilnikov and G. Cymbalyuk, *Phys. Rev. Lett.* **94**, 048101 (2005).

[5] A. Shilnikov, R. Gordon, I. Belykh, *Chaos* **18**, 037120 (2008).

[6] N. Kopell, D. Somers, *Biol. Cybern.* **68**, 5 (1993).

[7] R. Milo, S. Shen-Orr, S. Itzkovitz, N. Kashtan, D. Chklovskii, U. Alon, *Science* **298** (2002); M. I. Rabinovich, P. Varona, A. Selverston, and H. D. Abarbanel, *Rev. Modern Phys.* **78**, 4 (2006); O. Sporns and R. Kötter, *PLoS Biol.* **2**, 11 (2004).

[8] W.N. Frost and PS Katz, *PNAS* **93**, 422 (1996); A. G. M. Bulloch and N. I. Sayed, *Trends Neurosci.* **15**, 11 (1992); P. S. Katz and S. L. Hooper, in *Invertebrate Neuroscience* G. North and R. Greenspan (eds), (Cold Spring Harbor) (2007).

[9] G. B. Ermentrout, N. Kopell, *PNAS USA* **95** (1998); C. C. Canavier, D. A. Baxter, J. W. Clark, J. H. Byrne., *Biol. Cybern.* **80**, 87 (1999).

[10] P. Ashwin, G. P. King, J. W. Swift, *Nonlinearity* **3**, 3 (1990). C. Baesens, J. Guckenheimer, S. Kim , R. MacKay, Physica D **49**, 387, (1991).

[11] I. Belykh and A. Shilnikov, *Phys. Rev. Lett.* **101**, 078102 (2008).

[12] R. H. Clewley, W. E. Sherwood, M. D. LaMar, and J. M. Guckenheimer, http://pydstool.sourceforge.net (2006).

I. APPENDIX

A reduced model of the leech heart interneuron is given by the following set of three nonlinear coupled differential equations:

$$
\begin{aligned}
&C\,\frac{dV}{dt} = -I_{\rm Na} - I_{\rm K2} + I_{\rm L} - I_{\rm app} - I_{\rm syn},\\
&I_L = \bar{g}_{\rm L}\,(V - E_{\rm L}), \qquad I_{\rm K2} = \bar{g}_{\rm K2}\,m_{\rm K2}^2(V - E_{\rm K}),\\
&I_{\rm Na} = \bar{g}_{\rm Na}\,m_{\rm Na}^3\,h_{\rm Na}\,(V - E_{\rm Na}),\ quad m_{\rm Na} = m_{\rm Na}^{\infty}(V),\\
&\tau_{\rm Na}\,\frac{dh_{\rm Na}}{dt} = h_{\rm Na}^{\infty}(V) - h, \quad \tau_{\rm K2}\frac{dm_{\rm K2}}{dt} = m_{\rm K2}^{\infty}(V) - m_{\rm K2}.
\end{aligned}
$$

Here, $C = 0.5$nF is the membrane capacitance; V is the membrane potential in mV; I_{Na} is the sodium current with slow inactivation $h_{\rm Na}$ and fast activation $m_{\rm Na}$; $I_{\rm K2}$ is the slow persistent potassium current with activation $m_{\rm K2}$; $I_{\rm L}$ is the leak current and $I_{\rm app} = 0.006$ nA is an applied current. The values of maximal conductances are set as $\bar{\rm g}_{\rm K2} = 30$nS, $\bar{g}_{\rm Na} = 200$nS and $\rm g_L = 8$nS. The reversal potentials are $\rm E_{Na} = 0.045$ V, $\rm E_K = -0.07$ V and $E_{\rm L} = -0.046$ V. The time constants of gating variables are $\tau_{\rm K2} = 0.9$ sec and $\tau_{\rm Na} = 0.0405$ sec. The steady state values of gating variables, $h_{\rm Na}^{\infty}(V)$, $m_{\rm Na}^{\infty}(V)$, $m_{\rm K2}^{\infty}(V)$, are given by the following Boltzmann equations:

$$
\begin{aligned}
h_{\rm Na}^{\infty}(V) &= [1 + \exp(0.5(V + 0.325))]^{-1}\\
m_{\rm Na}^{\infty}(V) &= [1 + \exp(-0.15(V + 0.0305))]^{-1}\\
m_{\rm K2}^{\infty}(V) &= [1 + \exp\left(-0.083(V + 0.018 + {\rm V}_{\rm K2}^{\rm shift})\right)]^{-1}.
\end{aligned}
\tag{1}
$$

The synaptic current is modeled through the fast threshold modulation paradigm as follows:

$$
I_{\rm syn} = \sum_{j=1}^{n} \tilde{g}_{\rm syn}(1 \mp g_{\circlearrowleft})(E_{\rm syn}^{\rm inh} - V_i)]\Gamma(V_j - \Theta_{\rm syn}). \tag{2}
$$

The reversal potential $E_{\rm syn}^{\rm inh} = -0.0625$ is set to be smaller than $V_i(t)$, i.e. the synapse is inhibitory. The synaptic coupling function is modeled by the sigmoidal function $\Gamma(V_j) = 1/[1 + \exp\{-1000(V_j - \Theta_{\rm syn})\}]$. The threshold $\Theta_{\rm syn} = -0.03$ V is chosen so that every spike within a burst reaches it. This implies that the synaptic current from the presynaptic j-th neuron is initiated as soon as this neuron becomes active after its membrane potential exceeds the synaptic threshold.

The intrinsic bifurcation parameter V_{K2}^{shift} of the model is a deviation from $V_{1/2} = 0.018$ mV corresponding to the half-activated potassium channel at $m_{K2}^{\infty} = 1/2$. In the model (1), decreasing V_{K2}^{shift} delays the activation of m_{K2}. The bursting range of the bifurcation parameter of the given interneuron model is $[-0.024235, -0.01862]$; for smaller values of V_{K2}^{shift} the model enters the tonic spiking mode, or becomes hyperpolarizedly quiescent at the upper values. By varying V_{K2}^{shift} (or alternatively I_{app}) we can change the duty cycle of bursting (ratio [burst duration]/[burst period]) from 1 through 0. In this study, we use the values of $V_{K2}^{shift} = -0.01895$ mV, $V_{K2}^{shift} = -0.021$ mV and $V_{K2}^{shift} = -0.0225$ mV, corresponding to *short* (∼20%), *medium* (∼50%), and *long* (∼80%) bursting, respectively. Further details about the bifurcation underlying the transition between bursting and tonic spiking through the blue sky catastrophe, and the regulation of temporal characteristics of the bursting activity in this leech heart interneuron model can be found in [10].

Numerical methods

All numerical simulations and phase analysis were performed using the PyDSTool dynamical systems software environment (version 0.88) [12] http://pydstool.sourceforge.net. The software is freely available. Specific instructions and auxiliary files for the network (1) will be provided upon request.

The algorithm for constructing the 2D phase mappings from the 9D network model is based on the observation that two solutions $\mathbf{x}(t) = \psi(\mathbf{x_0}; t)$ and $\mathbf{x}(t) = \psi(\mathbf{x_0}; t+\tau)$ of an individual model can be considered as the same solution passing through the initial $\mathbf{x_0}$ on the T-periodic bursting orbit at different initial times. By releasing the solutions from $\mathbf{x_0}$ at different delays τ, ($0 < \tau < T$) we can generate a dense set of initial points which present a good first order approximation for the solutions of the network (1) in the case of sufficiently weak coupling.

Each sequence of phase lags $\{\Delta\phi_{31}^{(n)}, \Delta\phi_{21}^{(n)}\}$ plotted in Figs. 3–5 begins from an initial lag $(\Delta\phi_{31}^{(0)}, \Delta\phi_{21}^{(0)})$, which is the difference in phases measured relative to the recurrence time of cell 1 every time its voltage increases to a threshold $\Theta_{th} = -40$ mV. Θ_{th} marks the beginning of the spiking segment of a burst. As that recurrence time is unknown a priori due to interactions of the cells, we estimate it, up to first order, as a fraction of the period T_{synch} of the synchronous solution by selecting guess values $(\Delta\phi_{31}^{\star}, \Delta\phi_{21}^{\star})$. The synchronous solution corresponds to $\Delta\phi_{31} = \Delta\phi_{21} = 0$. By identifying $t = 0$ at the moment when $V_1 = \Theta_{th}$ with $\phi = 0$, we can parameterize this solution by time ($0 \le t < T_{synch}$) or by the phase lag ($0 \le \Delta\phi < 1$). For weak coupling and small lags, the recurrence time is close to T_{synch}, and $(\Delta\phi_{31}^{\star}, \Delta\phi_{21}^{\star}) \approx (\Delta\phi_{31}^{(0)}, \Delta\phi_{21}^{(0)})$. We use the following algorithm to distribute the true initial lags uniformly on a 40×40 square grid covering the phase portrait.

We initialize the state of cell 1 at $t = 0$ from the point (V^0, n^0, h^0) of the synchronous solution when $V_1 = \Theta_{th}$. Then, we create the initial phase-lagged state in the simulation by suppressing cells 2 and 3 for durations $t = \Delta\phi_{21}^0 T_{synch}$ and $\Delta\phi_{31}^0 T_{synch}$, respectively. On release, cells 2 and 3 are initialized from the initial point (V^0, n^0, h^0). We begin recording the sequence of phase lags between cells 2 and 3 and the reference cell 1 on the second cycle after coupling has adjusted the network period away from T_{synch}. In the case of stronger coupling (increased asymmetry via $g_{\circlearrowleft}$) where the gap between T_{synch} and the first recurrence time for cell 1 widens, we retroactively adjust initial phases using a "shooting" algorithm to make the initial phase lags sufficiently close to uniformly distributed positions on the square grid.